ACS Catalysis

pubs.acs.org/acscatalysis

Research Article

Tungsten Oxide-Based Z-Scheme for Visible Light-Driven Hydrogen Production from Water Splitting

Madasamy Thangamuthu,[⊥] Kiran Vankayala,[⊥] Lunqiao Xiong, Stuart Conroy, Xiaolei Zhang,* and Junwang Tang*

Cite This: *ACS Catal.* 2023, 13, 9113–9124

Read Online

ACCESS | Metrics & More | Article Recommendations | Supporting Information

ABSTRACT: The stoichiometric water splitting using a solar-driven Z-scheme approach is an emerging field of interest to address the increasing renewable energy demand and environmental concerns. So far, the reported Z-scheme must comprise two populations of photocatalysts. In the present work, only tungsten oxides are used to construct a robust Z-scheme system for complete visible-driven water splitting in both neutral and alkaline solutions, where sodium tungsten oxide bronze ($Na_{0.56}WO_{3-x}$) is used as a H_2 evolution photocatalyst and two-dimensional (2D) tungsten trioxide (WO_3) nanosheets as an O_2 evolution photocatalyst. This system efficiently produces H_2 (14 μmol h^{-1}) and O_2 (6.9 μmol h^{-1}) at an ideal molar ratio of 2:1 in an aqueous solution driven by light, resulting in a remarkably high apparent quantum yield of 6.06% at 420 nm under neutral conditions. This exceptional selective H_2 and O_2 production is due to the preferential adsorption of iodide (I^-) on $Na_{0.56}WO_{3-x}$ and iodate (IO_3^-) on WO_3, which is evidenced by both experiments and density functional theory calculation. The present liquid Z-scheme in the presence of efficient shuttle molecules promises a separated H_2 and O_2 evolution by applying a dual-bed particle suspension system, thus a safe photochemical process.

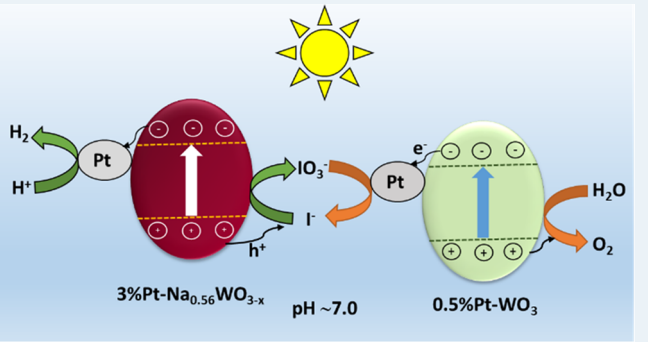

KEYWORDS: *green hydrogen, tungsten oxide, Z-scheme, visible photocatalysis, water splitting, DFT calculation*

1. INTRODUCTION

Hydrogen (H_2) production from earth-abundant water using sustainable solar energy is imperative to solve global energy demand and environmental issues.[1] Besides, solar H_2 is an alternative to gray H_2 derived from fossil fuels to be used in many industrial processes as feedstock including ammonia synthesis.[2,3] Solar-driven overall water splitting using semiconductor materials is one of the promising approaches to achieve sustainable production of H_2 in an economically viable manner.[4] However, the simultaneous production of H_2 and O_2 as an ideal process is extremely challenging in photocatalytic water splitting in the absence of an electric bias. A single photocatalyst with appropriate cocatalysts for pure water splitting has thus met with very limited success due to stringent bandgap requirements.[5,6] In parallel, there are many studies on the half-reaction of either proton reduction or water oxidation in the presence of an efficient but costly chemical scavenger. Typically, $BiVO_4$[7] or WO_3[8] for water oxidation and C_3N_4[9] or Rh dope $SrTiO_3$[10] for proton reduction were reported. A Z-scheme, also known as a dual photoexcitation system, akin to natural photosynthesis comprising H_2 evolution photocatalyst (HEP) and O_2 evolution photocatalyst (OEP), should be more efficient and economical for overall water splitting than the single photocatalyst with complicated cocatalysts.[11,12] It offers an extended choice of semiconductor materials with a narrow bandgap for both half-reactions, enabling it to achieve high solar-to-hydrogen conversion efficiency (STH). Furthermore, it has been predicted that a maximum of 12% STH can be achieved using a single absorber whereas it can be upraised significantly to 22% for Z-scheme-based systems due to much better visible light harvesting.[13] Typically, HEPs with the more negative conduction band (CB) potential concerning proton reduction (0.0 V vs NHE) and OEPs with the more positive valence band (VB) potential concerning water oxidation (1.23 V vs NHE) are suitable for H_2 and O_2 evolutions, respectively. The semiconductor particulate suspension-based Z-scheme system utilizing soluble redox mediator has been highly focused as it is much more simple and cost-effective than the solid Z-scheme,[14] and more importantly promises to produce H_2 and O_2 separately in a dual-bed particle suspension system

Received: March 22, 2023
Revised: June 9, 2023

https://doi.org/10.1021/acscatal.3c01312
ACS Catal. 2023, 13, 9113–9124

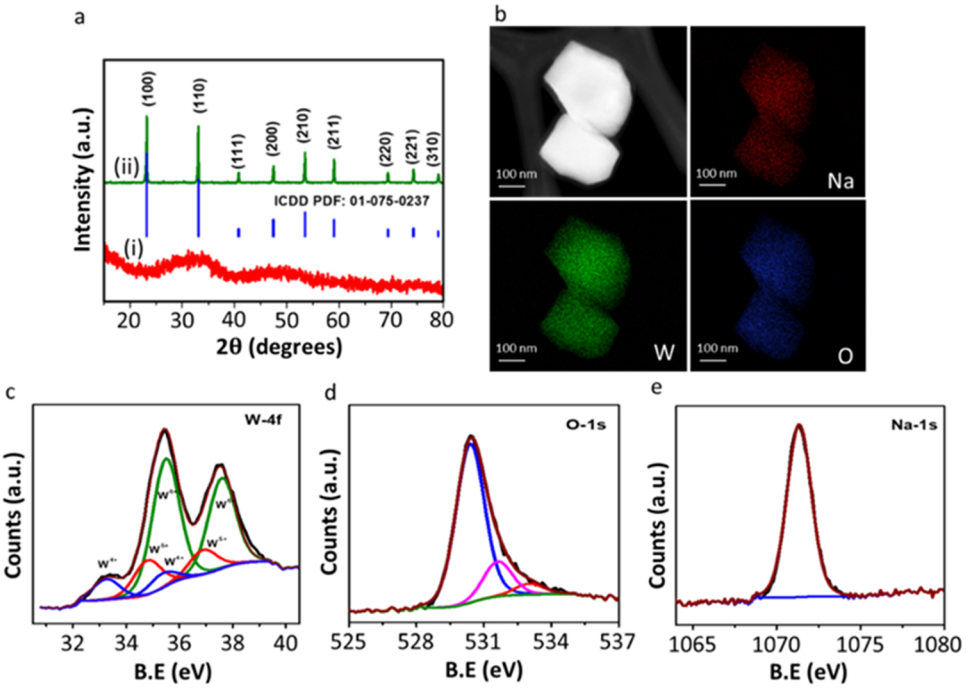

Figure 1. Characterization of HEP. (a) Powder XRD patterns of the (i) as-synthesized Na_xWO_{3-x} (NWO), a standard pattern of the cubic Na_xWO_{3-x} with PDF file no. 01-75-0237 (blue) and (ii) annealed Na_xWO_{3-x} ($Na_{0.56}WO_{3-x}$); (b) HAADF TEM image of $Na_{0.56}WO_{3-x}$ and the corresponding elemental mapping of Na (red), W (green), and O (blue); and (c−e) XPS spectra of W-4f, O-1s, and Na-1s regions in $Na_{0.56}WO_{3-x}$, respectively.

on a large scale, guaranteeing a safer chemical process compared with others, e.g., a solid Z-scheme.[13,15−17]

Several reports have successfully demonstrated the concept of dual semiconductor photocatalysts suspended in an aqueous solution containing redox couples such as $Fe^{3+}/^{2+}$, IO_3^- / I^-, I_3^-/I^-,[18,19] etc., as we have summarized in our recent review for light-assisted water splitting.[11] For example, Abe et al. accomplished an effective overall water splitting using Pt-TiO_2 (anatase) and Pt-TiO_2 (rutile) for H_2 and O_2 evolutions, respectively, in the presence of IO_3^-/I^- redox mediator, while under ultraviolet (UV) light.[20] Subsequently, several narrow-bandgap semiconductors viz. cation-doped $SrTiO_3$, graphitic carbon nitride (g-C_3N_4), $Sm_2Ti_2S_2O_5$, etc., as HEPs, and $BiVO_4$, WO_3, H_2WO_4, $AgNbO_3$, TaON, etc., as OEPs have been explored and implemented in a Z-scheme system to split water into stoichiometric amounts of H_2 and O_2.[4,21,22] Notably, surface-modified oxynitrides were described to improve the water splitting significantly by absorbing visible light effectively and suppressing the charge carrier recombination; however, oxynitrides are self-photocorrosive, leading to poor photostability.[23] In another report, a heterojunction based on oxynitrides (Pt-loaded $MgTa_2O_{6-x}$ N_y/TaON) as a HEP was shown to suppress charge carrier recombination, resulting in a drastic enhancement in overall water splitting with a benchmark apparent quantum yield (AQY) of 3.4% at 420 nm when considering a 2-electron process for H_2 production, in combination with PtO_x/WO_x as an OEP in the presence of IO_3^-/I^- as redox mediator.[24] Similarly, the AQY of a Z-scheme photocatalytic system at 420 nm was often measured.[10,25−29] Though substantial advances have been made so far, a significant breakthrough is yet to come. Hence, intensive research is underway by developing new materials[30] with special surface properties, high crystallinity, fewer defects,[31] spatial separation of reduction and oxidation sites, cocatalyst loading,[32] controlled morphology, heterojunction formation, etc., to achieve a high AQY.

Herein, we have developed a new tungsten oxide-only Z-scheme (WOZ) system for overall water splitting, in which both the HEP and OEP are tungsten oxides, i.e., sodium tungsten oxide bronze ($Na_{0.56}WO_{3-x}$) as the HEP and two-dimensional (2D) WO_3 nanosheets as the OEP in the presence of IO_3^-/I^- redox couple. Tungsten oxide-based materials have been widely studied but only as photoanodes or water oxidation photocatalysts due to their conduction band being too positive to meet proton reduction.[8,33,34] Moreover, WO_3 absorbs ∼12% of the solar spectrum and possesses a moderate hole-diffusion length (∼150 nm) in addition to impressive electron mobility (∼12 cm^2 V^{-1} s^{-1}).[34] Numerous stable nonstoichiometric WO_3 materials could be realized by altering the lattice oxygen vacancies to attain interesting optoelectronic/catalytic properties. To the best of our knowledge, a Z-scheme system composed of one type of oxide photocatalysts for visible-driven-pure water splitting has not been reported. Very recently upraising the CB position of WO_x to a more negative potential was shown, e.g., by creating oxygen vacancies[35] or surface defects engineering.[36] Here, we prepared a new and stable WO_x-based HEP, $Na_{0.56}WO_{3-x}$. Interestingly, it can be coupled with WO_3 nanosheets as an OEP to form a robust Z-scheme, which demonstrates efficient pure water splitting under light irradiation. Compared with the bulk materials, WO_3 nanosheets provide more exposed active sites due to their sheet-like morphology. Such a novel Z-scheme generates H_2 and O_2 stoichiometrically, demonstrating a high AQY of 6.06% at 420 nm, under light irradiation and ambient conditions.

https://doi.org/10.1021/acscatal.3c01312
ACS Catal. 2023, 13, 9113−9124

2. RESULTS AND DISCUSSION

2.1. Characterization of the Photocatalysts. *2.1.1. Hydrogen Evolution Photocatalyst (HEP).* Na_xWO_{3-x} was prepared under ambient conditions by treating sodium tungstate with sodium borohydride (see details in the Experimental Section). The obtained powders were characterized using various physicochemical techniques. Figure 1a shows the powder XRD patterns of the as-synthesized samples and samples annealed at 800 °C under a N_2 atmosphere. It is clearly seen that the as-synthesized sample is amorphous as it has very broad diffraction peaks. However, the annealed sample exhibits sharp strong peaks, indicating that annealing imparted crystallinity to the sample, as expected. These peaks can be assigned to the cubic Na_xWO_{3-x} (*Pm*-3*m*) (Figure S1), matching well with the standard pattern (PDF No. 01-75-0237). The Na content present in the annealed Na_xWO_{3-x} was determined to be around 0.56 using a microwave plasma-atomic emission spectrometer, which is also verified using the experimentally (XRD) measured lattice parameter (a_o) according to the eq 1,[37,38] so this sample is denoted $Na_{0.56}WO_{3-x}$.

$$a_o(\text{Å}) = (3.7845 + 0.0820x) \quad (1)$$

Figure S2 represents transmission electron microscopy (TEM) images of the as-synthesized HEP, indicating that the sample is composed of interconnected spheres with dimensions around 100−150 nm. The high-resolution TEM (HRTEM) image of the as-synthesized sample shows the absence of crystallinity, demonstrating the amorphous nature. After annealing, the amorphous sample becomes crystalline, which is obvious from the TEM image (Figure S3), and the Pt nanoparticles distribution on the surface of the $Na_{0.56}WO_{3-x}$ reveals the successful cocatalyst loading. Furthermore, the new crystalline $Na_{0.56}WO_{3-x}$ lattice was identified as (100), and the photodeposited Pt nanoparticles show (200) lattice (Figure S4). The elemental mapping of $Na_{0.56}WO_{3-x}$ shows the uniform distribution of Na, W, and O elements (Figure 1b). The surface oxidation states of $Na_{0.56}WO_{3-x}$ were assessed using X-ray photoelectron spectroscopy (XPS). The survey spectrum is shown in Figure S5. Figure 1c−e represents the deconvoluted core-level XPS spectra of W-4f, O-1s, and Na-1s recorded for $Na_{0.56}WO_{3-x}$. As shown in Figure 1c, the presence of three doublets ($4f_{7/2}$ and $4f_{5/2}$) in the W-4f spectra of $Na_{0.56}WO_{3-x}$ unveils the presence of tungsten in multiple oxidation states. For instance, it shows peaks at binding energy (BE) values around 33.3 and 35.4 eV, 34.8 and 36.9 eV, and 35.5 and 37.6 eV. The first set of doublets corresponds to the presence of W^{4+}, while the second and third doublets disclose the presence of W^{5+} and W^{6+} species, respectively. The deconvoluted O-1s XPS consists of three peaks at BE values 530.4, 531.6, and 533.1 eV[37] (Figure 1d). The most intense peak at 530.4 eV is attributed to lattice oxygen (O^{2-}) surrounded by W atoms in the $Na_{0.56}WO_{3-x}$ lattice. The origin of the peak at 531.6 eV is due to oxygen (OH^-) (the adsorbed OH^-) in the regions of oxygen vacancies (due to W^{5+}/W^{4+} species) within the $Na_{0.56}WO_{3-x}$ matrix. In these oxygen-deficient sites, OH groups are known to bond with metal cations to compensate for the charge. The peak located at 533.1 eV could be due to the presence of adsorbed H_2O on the surface of $Na_{0.56}WO_{3-x}$.[37] The deconvoluted Na-1s XPS shows a single peak at 1071.2 eV (Figure 1e), in agreement with an earlier study.[39] A similar set of peaks are observed after cocatalyst Pt loading, Pt- $Na_{0.56}WO_{3-x}$ (see Table S1).

2.1.2. Oxygen Evolution Photocatalyst (OEP). 2D WO_3 nanosheets as an OEP in the Z-scheme system were obtained by thermal annealing of 2D tungstic acid ($WO_3{\cdot}H_2O$) under an air atmosphere at 500 °C (see the Experimental Section for details). The conversion of tungstic acid into tungsten trioxide was studied using XRD and Raman spectroscopy. The powder XRD pattern of WO_3 nanosheets along with its precursor $WO_3{\cdot}H_2O$ are shown in Figure 2a. The as-synthesized $WO_3{\cdot}H_2O$ nanosheets are crystalline and the XRD pattern matches well with the standard pattern (PDF No: 01-084-0886) for orthorhombic (*Pmnb*) hydrated WO_3 with strong diffraction peaks for (111), (020), and (131) planes, in agreement with the earlier report.[40]

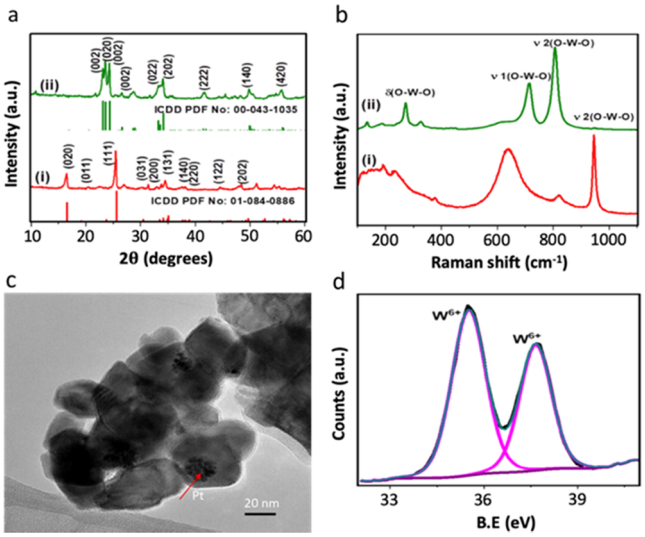

Figure 2. Characterization of OEP. (a) XRD patterns of (i) as-synthesized $WO_3{\cdot}H_2O$ and (ii) annealed (WO_3 nanosheets) samples and their corresponding standard ICDD patterns; (b) Raman spectra of (i) $WO_3{\cdot}H_2O$ and (ii) WO_3 nanosheets recorded using a 532 nm green laser; (c) TEM image of Pt-WO_3 and the presence of Pt nanoparticles on the surface of WO_3 is indicated with an arrow; and (d) XPS spectra corresponding to the W-4f region of WO_3 nanosheets.

After annealing it in the air at 500 °C for 3 h, the formation of monoclinic (*P21/n*) WO_3 nanosheets is observed, corresponding to the standard pattern (PDF No: 00-043-1035). It confirms the transformation of orthorhombic $WO_3{\cdot}H_2O$ into monoclinic WO_3 due to annealing (Figure S6). This phenomenon is further verified by Raman spectroscopy, as shown in Figure 2b. The Raman spectra of $WO_3{\cdot}H_2O$ show three peaks at ∼642, ∼820, and ∼946 cm^{-1}, corresponding to the first W−O−W, [ν1(W−O−W)], second W−O−W [ν2(W−O−W)], and terminal W═O stretching vibrations, respectively. The sharp peaks at ∼642 and ∼946 cm^{-1} confirm that the as-synthesized nanosheets are hydrated WO_3 ($WO_3{\cdot}H_2O$). The Raman spectra of WO_3 nanosheets (Figure 2b) show two major peaks at ∼714 and ∼808 cm^{-1}, corresponding to the W−O−W stretching modes, confirming the formation of monoclinic WO_3. The other notable difference in WO_3 nanosheet spectra is the absence of terminal W═O stretching mode at 946 cm^{-1} compared to $WO_3{\cdot}H_2O$. Besides, a strong peak appears at 272 cm^{-1} along with two low intense peaks at around 192 and 325 cm^{-1}, which are corresponding to W−O−

https://doi.org/10.1021/acscatal.3c01312
ACS Catal. 2023, 13, 9113−9124

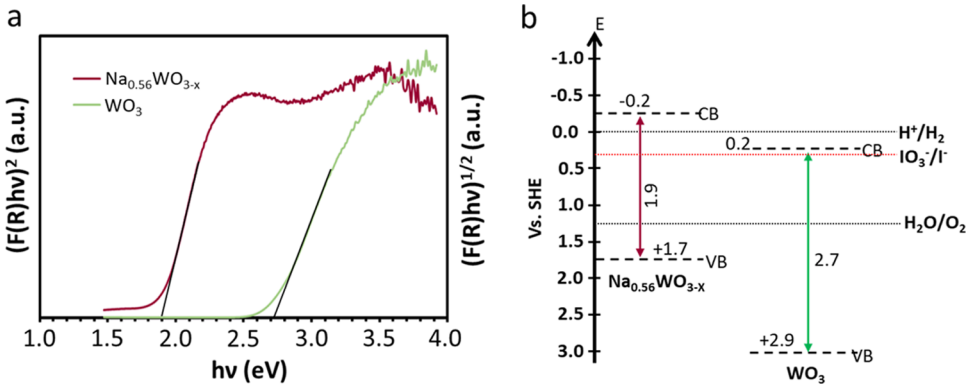

Figure 3. (a) Tauc plots of WO_3 nanosheets, an indirect bandgap semiconductor, and $Na_{0.56}WO_{3-x}$, a direct bandgap semiconductor; (b) the proposed band diagram for $Na_{0.56}WO_{3-x}$- and WO_3-based Z-scheme photocatalytic water splitting system vs SHE.

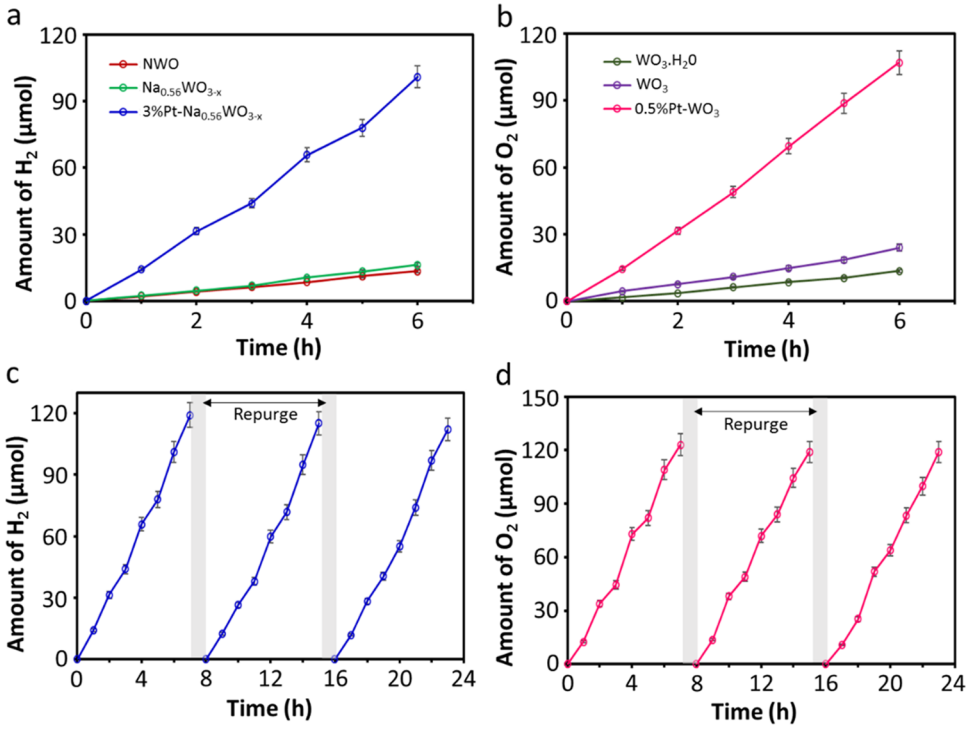

Figure 4. Photocatalytic H_2 and O_2 evolution half-reactions. (a) H_2 evolution from water (pH 7.0) using 10 mg of NWO-based materials (NWO, $Na_{0.56}WO_{3-x}$, and 3wt%Pt-$Na_{0.56}WO_{3-x}$) containing 5 mM NaI as a hole scavenger under a full-arc condition for 6 h; (b) O_2 evolution from water (pH 8.5) using 10 mg of WO_3-based materials ($WO_3{\cdot}H_2O$, WO_3 nanosheets, and 0.5%Pt-WO_3 nanosheets) containing 5 mM $NaIO_3$ as an electron scavenger under a full-arc condition for 6 h; (c) the H_2 evolution stability study on 3%Pt-$Na_{0.56}WO_{3-x}$ in an aqueous solution (pH 7.0) containing 5 mM NaI under a full-arc condition for three consecutive 7 h runs; and (d) the O_2 evolution stability study on 0.5%Pt-WO_3 nanosheets in an aqueous solution (pH 8.5) containing 5 mM $NaIO_3$ under a full-arc condition for three 7 h runs; Ar gas was purged after each run.

W bending modes of WO_3.[41] The ratio of $I_{\nu 2(W\text{-}O\text{-}W)}/I_{\nu(W{=}O)}$ can provide information about x in $WO_3{\cdot}xH_2O$ as suggested earlier.[40] As expected the ratio is lower for $WO_3{\cdot}H_2O$, while it is higher for WO_3 nanosheets, validating the dehydration of $WO_3{\cdot}H_2O$. The layered morphology of $WO_3{\cdot}H_2O$ nanosheets is evident from the TEM images, as shown in Figure S7. The EDX spectra validate that the material is mainly made of W and O elements. Figure 2c shows the TEM image of Pt-WO_3, which shows the presence of Pt nanoparticles on the surface of the WO_3 mixture composed of nanosheets and nanoparticles (denoted WO_3 nanosheets afterward). The deconvoluted W-4f XPS of WO_3 shown in Figure 2d displays a doublet at BE values 37.5 and 37.6 eV suggesting that the W is present at +6 oxidation state only. These results suggest that W has a single oxidation state in WO_3. The presence of W^+6 also confirms the formation of WO_3 upon annealing of $WO_3{\cdot}H_2O$, complementing XRD, and Raman measurements.

2.1.3. Band Structure of HEP and OEP. UV−Vis diffuse reflectance spectroscopy (DRS) was used to disclose the bandgap of the investigated photocatalysts. The optical absorbance spectra of $Na_{0.56}WO_{3-x}$ and WO_3 nanosheets are shown in Figure S8. It is clearly seen that both materials absorb visible light efficiently and the Tauc plots of $Na_{0.56}WO_{3-x}$ and WO_3 (Figure 3a) reveal a bandgap of 1.9 and 2.7 eV, respectively. To explicitly determine the band positions, we have measured the CB by photoelectrochemistry and Mott−Schottky measurement. The photocurrent onset potential measurement results are shown in Figure S9. The measured

https://doi.org/10.1021/acscatal.3c01312
ACS Catal. 2023, 13, 9113−9124

potential against Ag/AgCl was converted to SHE using $E_{(SHE)} = E_{Ag/AgCl} + E_{Ag/AgCl}^{0}$. The WO_3 has a CB potential of +0.2 V, which is consistent with the reported[42] and the $Na_{0.56}WO_{3-x}$ has CB at −0.2 V. To validate it further, we have tested the CB potential of the $Na_{0.56}WO_{3-x}$ and WO_3 using the Mott−Schottky method (Figure S10), and the observed results agree with the photocurrent onset potential measurement. In addition, we have performed a control experiment to test the water oxidation property of $Na_{0.56}WO_{3-x}$ in the presence of IO_3^- and observed a tiny amount of O_2 evolved (0.3 μmol h^{-1}), 60 times less active compared to WO_3 (17.9 μmol h^{-1}). Such a small O_2 evolution rate of $Na_{0.56}WO_{3-x}$ reveals the less positive VB potential of $Na_{0.56}WO_{3-x}$ compared to WO_3. Thus, it is essential to engineer a Z-scheme composed of $Na_{0.56}WO_{3-x}$ and WO_3 for complete water splitting. Accordingly, the energy band diagram was drawn, as shown in Figure 3b. The CB of WO_3 is too positive to reduce protons into H_2, which is essential to form an efficient Z-scheme system as it is close to the VB of the HEP when coupling $Na_{0.56}WO_{3-x}$ with WO_3. The deep VBM of WO_3 nanosheets and negative CBM of $Na_{0.56}WO_{3-x}$ suggest that it is highly suitable for water oxidation, and reduction reactions, respectively. More importantly, these well-matched band positions promise a new Z-scheme composed of tungsten oxides.

2.2. Photocatalytic H_2 Evolution. To verify the photocatalytic ability of $Na_{0.56}WO_{3-x}$-based materials for H_2 production, experiments were performed in aqueous solutions containing NaI (pH ∼7.0) as a hole scavenger under Xe lamp irradiation, and the results are shown in Figure 4a. The compelling observation from Figure 4a is that the NWO and $Na_{0.56}WO_{3-x}$ can produce H_2 without any cocatalysts, which is otherwise difficult with WO_3-based materials due to the inappropriate CB position concerning the H_2 evolution potential, suggesting that both NWO and $Na_{0.56}WO_{3-x}$ can be used as a photocatalyst for H_2 production from water. Both NWO (amorphous) and $Na_{0.56}WO_{3-x}$ (crystalline) photocatalysts produce H_2 at a rate of 2.2 and 2.5 μmol h^{-1}, respectively. Subsequently, the effect of pH on H_2 evolution was studied to optimize the condition at which NWO-based materials yield higher rates of H_2 production. As shown in Figure S11, the $Na_{0.56}WO_{3-x}$ shows better activity than NWO from neutral to weakly alkaline solution, where the H_2 evolution rate was obtained from the first 6 h run. Furthermore, we have tested the chemical stability of $Na_{0.58}WO_{3-x}$ for H_2 evolution at pH 8.5 and 10.5 by running four 6 h reaction cycles (Figure S12). The initial rate of H_2 evolution does not change significantly at both pH values, but from the third cycle onward, the H_2 evolution rate starts to reduce and saturates in the fourth cycle only at pH 10.5. This suggests that the present HEP is highly stable under a weakly alkaline condition but not stable at a strong alkaline condition for a prolonged run. Hence, well-crystallized $Na_{0.56}WO_{3-x}$ was selected for further studies. To improve the activity, 3wt%-Pt (cocatalyst) particles were loaded on the surface of $Na_{0.58}WO_{3-x}$ by photodeposition (see Experimental Section for details), which significantly improves the H_2 evolution to a rate of 16.8 μmol h^{-1} at pH 7.0. It is worth noting that after loading the cocatalyst (3%Pt-$Na_{0.56}WO_{3-x}$), the best activity was observed at pH 7.0. This is anticipated as the cocatalysts extract the electron efficiently and minimize the recombination with holes. The H_2 evolution reaction in the presence of I^- ions at pH 7.0 can be represented by the following equations.

$$Pt - Na_xWO_3 \xrightarrow{h\nu} e^- + h^+ \quad \text{(Photoexcitation)} \tag{2}$$

$$3I^- + 2h^+ \rightarrow I_3^- \quad \text{(Oxidation of } I^- \text{ to } I_3^- \text{ in acidic solution)} \tag{3}$$

$$I^- + 6OH^- + 6h^+ \rightarrow IO_3^- + 3H_2O \quad \text{(Oxidation of } I^- \text{ to } IO_3^- \text{ in alkaline solution)} \tag{4}$$

$$2H^+ + 2e^- \rightarrow H_2 \quad \text{(Reduction of } \textit{protons} \text{ by } \textit{electrons}\text{)} \tag{5}$$

The stability of the 3%Pt-$Na_{0.56}WO_{3-x}$ for prolonged H_2 evolution was investigated by measuring the H_2 evolution for 21 h (composed of three consecutive 7 h runs) and no significant change in the H_2 evolution rate is observed, as shown in Figure 4c, suggesting the robustness of $Na_{0.56}WO_{3-x}$ under neutral pH. We further validated the stability of the HEP by testing the compositional changes using XPS after three consecutive photocatalytic runs, as shown in Figure S13. No obvious changes were observed in the deconvoluted spectra of O-1S and Na-1S; however, a small reduction in the W^{4+} signal was observed, while the signals for W^{5+} and W^{6+} are stable. The identical H_2 evolution suggests that W^{5+} and W^{6+} are the species dominating water reduction under the present experimental conditions. Furthermore, the XRD spectra of the 3%Pt-$Na_{0.56}WO_{3-x}$ before and after the photocatalysis show (Figure S14a) no significant changes, which again confirms the robustness of the HEP under neutral pH.

2.3. Photocatalytic O_2 Evolution. Subsequently, we investigated the photocatalytic O_2 evolution half-reaction using WO_3 under a full-arc condition in water containing IO_3^- ions as a sacrificial electron acceptor. As expected, a significant amount of O_2 evolution was observed at ∼pH 8.5 using both $WO_3{\cdot}H_2O$ and WO_3, but monoclinic WO_3 nanosheets show better activity than orthorhombic $WO_3{\cdot}H_2O$ (Figure 4b). Thereafter, WO_3 nanosheets were loaded with 0.5 wt % Pt cocatalyst (Pt-WO_3), leading to an O_2 evolution rate of 17.9 μmol h^{-1}, which is superior to cocatalyst-free WO_3 (3.8 μmol h^{-1}) and $WO_3{\cdot}H_2O$ (2.2 μmol h^{-1}). The present Pt-WO_3 water oxidation activity is comparable to the best activity reported previously,[43−45] thanks to the advantages of nanosheet morphology. The O_2 evolution using Pt-WO_3 from weakly alkaline water containing IO_3^- ions can be represented by the following equations.

$$Pt - WO_3 \xrightarrow{h\nu} e^- + h^+ \quad \text{(Photoexcitation)} \tag{6}$$

$$IO_3^- + 3H_2O + 6e^- \rightarrow I^- + 6OH^- \quad \text{(Reduction of } IO_3^- \text{ by electrons)} \tag{7}$$

$$4OH^- \rightarrow O_2 + 4e^- + 2H_2O \quad \text{(Water oxidation)} \tag{8}$$

In the absence of a photocatalyst or an electron acceptor (IO_3^-), no O_2 evolution is observed. The H_2 evolution activity of the Pt-WO_3 was also monitored using I^- as the hole scavenger to examine the suitability of WO_3 for a potentially efficient Z-scheme for water splitting. As anticipated, negligible H_2 evolution is observed (Figure S15), in agreement with the CB position of WO_3 measured in Figure 3d, which is not appropriate for water reduction, suggesting that the Pt-WO_3 is highly selective for the water oxidation half-reaction. The stability of Pt-WO_3 nanosheets for prolonged O_2 evolution at pH 8.5 was examined for 21 h (composed of 3 consecutive 7-h

https://doi.org/10.1021/acscatal.3c01312
ACS Catal. 2023, 13, 9113−9124

Table 1. Photocatalytic Water Splitting over the WO_x Catalysts (Runs 3 to 7, and 10: 10 mg of HEP and 5 mg of OEP, runs 8, 9, and 11: 5 mg of HEP and 5 mg of OEP) Suspended in an Aqueous Solution Performed under Different Experimental Conditions

run	HEP	OEP	mediator	pH	weight ratio	HER (μmol h^{-1})	OER (μmol h^{-1})
1	3%Pt-$Na_{0.56}WO_{3-x}$	-	NaI	7.0	-	16.8	-
2	-	0.5%Pt-WO_3	$NaIO_3$	8.5	-	-	17.9
3	3%Pt-$Na_{0.56}WO_{3-x}$	0.5%Pt-WO_3	$NaIO_3$	7.0	2:1	-	11.3
4	3%Pt-$Na_{0.56}WO_{3-x}$	0.5%Pt-WO_3	NaI	3.0	2:1	3.0	-
5	3%Pt-$Na_{0.56}WO_{3-x}$	0.5%Pt-WO_3	$FeCl_2$	3.0	2:1	2.8	-
6	3%Pt-$Na_{0.56}WO_{3-x}$	0.5%Pt-WO_3	NaI	7.0	2:1	14.6	4.8
7	3%Pt-$Na_{0.56}WO_{3-x}$	0.5%Pt-WO_3	NaI	8.5	2:1	13.9	5.3
8	3%Pt-$Na_{0.56}WO_{3-x}$	0.5%Pt-WO_3	NaI	7.0	1:1	14.0	6.9
9	3%Pt-$Na_{0.56}WO_{3-x}$	0.5%Pt-WO_3	NaI	10.5	1:1	10.7	7.9
10	3%Pt-$Na_{0.56}WO_{3-x}$	0.5%Pt-WO_3	NaI	10.5	2:1	9.6	4.9
11	3%Pt-$Na_{0.56}WO_{3-x}$	0.5%Pt-WO_3	-	7.0	1:1	-	-

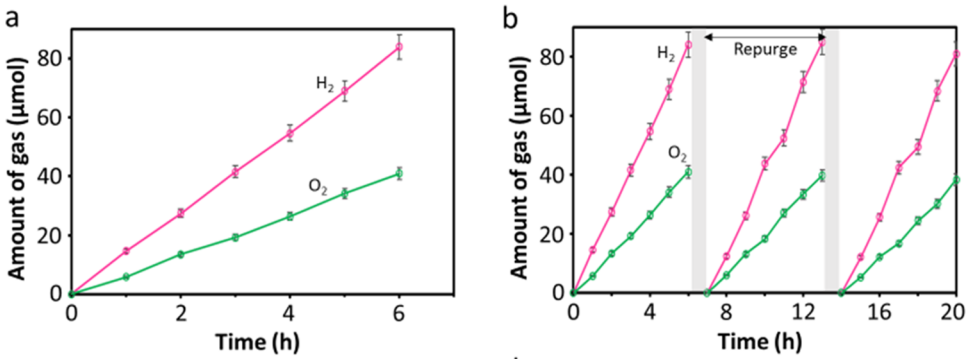

Figure 5. Stoichiometric water splitting with error bar after three measurements. (a) WOZ water splitting system composed of 10 mg of 3wt%Pt-$Na_{0.56}WO_{3-x}$ as the HEP and 10 mg of 0.5wt%Pt-WO_3 nanosheets as the OEP under the full-arc condition at pH 7.0 and 5 mM NaI as a redox mediator; (b) the stability study on 3wt%Pt-$Na_{0.56}WO_{3-x}$−NaI−0.5wt%Pt-WO_3 under the same photocatalytic conditions for three successive 6 h runs.

runs), and no significant decrease in O_2 evolution rate is observed, as shown in Figure 4d, suggesting that WO_3 is a robust photocatalyst under weakly alkaline conditions. In addition, no changes were observed in the XRD of Pt-WO_3 before and after photocatalysis (Figure S14b), which further ensures stability. Furthermore, we also tested the stability of WO_3 at pH 10.5 and observed no change in the beginning of the reaction, similar to the HEP, but over a prolonged run, the O_2 evolution rate was significantly reduced (Figure S16). This strongly suggests that the present OEP is stable only under weak alkaline pH and not stable in strong alkaline solutions.

2.4. Z-Scheme Overall Water Splitting. The overall water splitting activity of the new Z-scheme system composed of only tungsten oxides, i.e., 3%Pt-$Na_{0.56}WO_{3-x}$ as the HEP and 0.5%Pt-WO_3 as the OEP was then tested under full-arc as well as visible light conditions. When each photocatalyst is tested independently, only H_2 or O_2 evolution was observed (Table 1, run 1 and 2). When the system is composed of both the HEP and OEP in an aqueous solution containing I^- as a redox mediator, the successful evolution of H_2 and O_2 was observed simultaneously (Table 1, run 6). In the case of an aqueous solution containing IO_3^- as a redox mediator, the simultaneous evolution of H_2 and O_2 was not observed. Instead, only O_2 evolution was noted (Table 1, run 3), suggesting that the reduction of IO_3^- to I^- is slower, either because I^- cannot desorb easily from the OEP or IO_3^- reduction strongly competes with proton reduction to H_2, which will be discussed later. Both H_2 and O_2 production rates are highly dependent on the pH of the solution, which is shown in Table 1 that at pH ∼3.0 acidic condition, poor H_2 and no O_2 evolutions were observed in the I^- aqueous solution (Table 1, run 4). This could be due to the oxidation of I^- to mainly I_3^-, which is a poor electron scavenger compared to IO_3^- at pH 3.0, as listed in eq 3 against eq 4, and is preferable in a neutral/alkaline solution and in turn hinders the establishment of the IO_3^-/I^- redox system.[46] Similar results were observed while using Fe^{2+} as a redox mediator (Table 1, run 5). At pH ∼7.0, in the presence of I^-, the evolution of both H_2 and O_2 gases was attained (Table 1, run 6); however, the stoichiometric ratio of H_2 to O_2 has not been achieved. Further, when the reactions were carried out at pH ∼8.5 (Table 1, run 7), simultaneous productions of H_2 and O_2 were observed; however, yet again in nonstoichiometric quantities. Subsequently, we performed optimization studies by varying the weight ratio of HEP to OEP at pH ∼7.0. A weight ratio of 1:1 (HEP:OEP, by weight) has been found to produce H_2 and O_2 gases simultaneously with a rate of 14 μmol h^{-1} (2800 μmol h^{-1} g^{-1}) and 6.9 μmol h^{-1} (1380 μmol h^{-1} g^{-1}), respectively, at a stoichiometric molar ratio of 2:1 (Table 1, run 8).

The temporal gas evolution is shown in Figure 5a and the consecutive run is represented in Figure 5b, suggesting that the present system is not only efficient but also rather stable under the present experimental conditions. We also tested the present WO_x-based Z-scheme (WOZ) activity at pH 10.5 and observed no stoichiometric gas evolution at a 1:1 mass ratio

https://doi.org/10.1021/acscatal.3c01312
ACS Catal. 2023, 13, 9113−9124

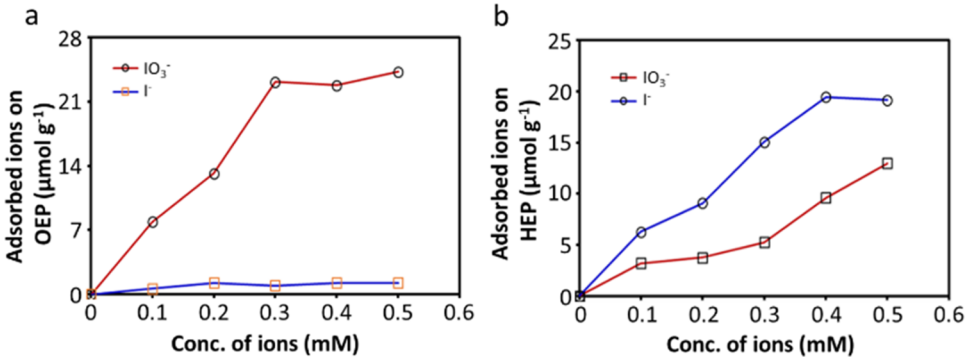

Figure 6. Adsorption study. (a) Adsorption behavior of IO_3^- and I^- anions on the surface of 0.5wt%Pt-WO_3 (OEP) powder suspended in an aqueous solution at pH ∼8.5 under dark conditions; (b) adsorption behavior of IO_3^- and I^- anions on 3wt%Pt-$Na_{0.56}WO_{3-x}$ (HEP) powder suspended in an aqueous solution at pH ∼7.0 under dark conditions.

(Table 1, run 9), whereas at a mass ratio of 2:1, stoichiometric gas evolution was observed (Table 1, run 10), proving that the tungsten oxide-based Z-scheme can split water at both neutral and weakly alkaline conditions. In the absence of a redox mediator (Table 1, run 11), no gas evolution was observed, indicating that the I^- is crucial for the Z-scheme. The performance of the present Z-scheme water splitting system under visible-light irradiation ($\lambda \geq 420$ nm) was also measured, as shown in Figure S17. Again, the simultaneous production of H_2 and O_2 with a rate of 7.4 and 3.6 μmol h^{-1} is monitored, and the gas amount produced remains almost linear increase with time. The H_2 production activity of the $Na_{0.56}WO_{3-x}$ has been tested under half-reaction conditions at higher wavelengths using 600 and 650 nm monochromatic filters. The obvious H_2 evolution was observed under half-reaction conditions with a rate of 0.9 and 0.27 μmol h^{-1}, respectively (Figure S18), but under Z-scheme working conditions, pure water splitting was not observed (generation of both H_2 and O_2) as WO_3 is silent at these very long wavelengths. The AQY for H_2 production from water using the proposed WOZ system was assessed three times and the average was reported. At 420 nm, an AQY of 6.06% (Figure S19) for water splitting was determined by considering the 2-electron process involved for one molecule of H_2 evolution (see Experimental Section for details, and in some works of the literature, the 4-electron process was used to calculate the AQY.[47] Using that method, the AQY is 12% herein). The H_2 and O_2 evolution rates under 420 nm monochromatic irradiation are shown in Figure S20. The Z-scheme photocatalytic activity of the present works was compared with the reported representative studies (Table S2).

2.5. Adsorption Studies. As the current Z-scheme works very efficiently, we investigated the shuttle molecule's function in detail. First, both HEP and OEP were tested for H_2 production in the presence of hole scavenger I^- (Figure S15). One can see that the H_2 is produced on the 3%Pt-$Na_{0.56}WO_{3-x}$ but not on the 0.5%Pt-WO_3 nanosheets, proving that the CB of WO_3 nanosheets is not appropriate for proton reduction while the CB of $Na_{0.56}WO_{3-x}$ is negative enough to reduce the proton to H_2 (Figure 3d). The selectivity of the OEP, 0.5%Pt-WO_3 for the O_2 evolution half-reaction is then verified, where I^- oxidation ($I^- \rightarrow IO_3^-$) might compete with water oxidation by consuming the photogenerated holes from the OEP. We examined this by adding 1 mM I^- anions at 3 h during the ongoing water oxidation half-reaction in an aqueous solution (pH ∼8.5) containing 5 mM IO_3. Interestingly, no influence was observed by the extra I^- anions on the water oxidation reaction (Figure S21), strongly indicating that the nanosheets OEP can produce O_2 highly selectively even in the presence of efficient hole scavenger I^-. To disclose the reason behind this, we have studied the adsorption behavior of IO_3^- and I^- anions onto the OEP by measuring their concentrations before and after the addition of 0.5%Pt-WO_3 powder to the solution under dark conditions (see Experimental Section for details).

As shown in Figure 6a, the IO_3^- ions are adsorbed preferentially onto the OEP surface whereas I^- shows poor adsorption, confirming that the water oxidation is dominant on the OEP rather than the oxidation of I^- to IO_3^-. On the other hand, the crucial IO_3^- ions reduction is guaranteed due to their strong adsorption. Therefore, the couple of IO_3^-/I^- is the ideal charge mediator for a Z-scheme containing the WO_3 nanosheets. Similarly, we also tested the competitive reaction between water reduction and IO_3^- reduction ($IO_3^- \rightarrow I^-$) driven by the photogenerated electrons on 3%Pt-$Na_{0.56}WO_{3-x}$, HEP. As shown in Figure S22, we added two distinct concentrations of IO_3^- (100 μM and 1 mM) after 3 h during the ongoing water reduction half-reaction and noticed no significant change upon the addition of 100 μM of IO_3^-. However, a substantial deceleration of H_2 evolution was observed when adding 1 mM IO_3^-. These results suggest that at higher IO_3^- concentrations, the photogenerated electrons from the HEP are also consumed by IO_3^- ions, in good agreement with the earlier report[20] where a similar phenomenon was observed.

To understand further, we observed the competitive adsorption behavior of I^- and IO_3^- on 3%Pt- $Na_{0.56}WO_{3-x}$. As shown in Figure 6b, both I^- and IO_3^- anions are adsorbed on the surface of the HEP, but I^- ions show relatively high preference, which is also proved by our XPS measurement of the used photocatalyst (Figure S13a) and is crucial for the Z-scheme water splitting. The adsorption behavior of I^- and IO_3^- anions on bare $Na_{0.56}WO_{3-x}$ was also undertaken (Figure S23). It is obvious that the I^- ions are preferentially adsorbed especially at low concentrations. Therefore, the sufficient adsorption of I^- on $Na_{0.56}WO_{3-x}$ enables to accept the photogenerated holes, reducing the recombination with photogenerated electrons and hence promoting the selective H_2 evolution. However, beyond 1 mM concentration, IO_3^- adsorption is dominated. Hence, in the presence of excess IO_3^- ions, H_2 evolution is limited, which agrees well with our control experiment (Figure S22). We also found out that only

https://doi.org/10.1021/acscatal.3c01312
ACS Catal. 2023, 13, 9113−9124

O_2 is produced in the WOZ with only the IO_3^- mediator (Table 1, run 3), wherein one can see the reason that IO_3^- can relatively easily adsorb on the HEP (Figure 6b) and its reduction strongly competes with proton reduction (Figure S22). Therefore, controlling the concentration of IO_3^- ions in the WOZ is one key issue, which from another angle proves that the initial addition of only I^- mediator instead of both I^- and IO_3^- mediators is of importance as demonstrated in our experimental design. We also found that continuous production of H_2 and O_2 for a prolonged time in our WOZ is stable and reproducible and the concentration of I^- and pH were observed to be constant, demonstrating a highly selective and efficient Z-scheme system. A similar experimental study was reported previously[48] in which the selective adsorption of IO_3^- anion on WO_3 (OEP) was observed, leading to the selective O_2 evolution reaction.

To consolidate the adsorption behavior observed experimentally, the redox molecules' adsorption on photocatalysts was also studied by DFT calculation. The description of the model for WO_3Pt_4 and $Na_{0.625}WO_{2.875}Pt_4$ is detailed in the Supporting Information. IO_3^- and I^- were adsorbed onto each catalyst at two sites: over the platinum cluster and directly onto the surface of the catalyst. The optimized catalyst models, as well as the adsorption models, can be seen in Figures S24–S31. Adsorption energies are calculated using eq 9, where E represents the enthalpy, A is the adsorbent, B is the adsorbate, and AB is the complex structure.

$$E_{ads} = -E_{AB} + (E_A + E_B) \quad (9)$$

The calculated adsorption energies for each tested adsorption site are shown in Figure 7. It can be seen that,

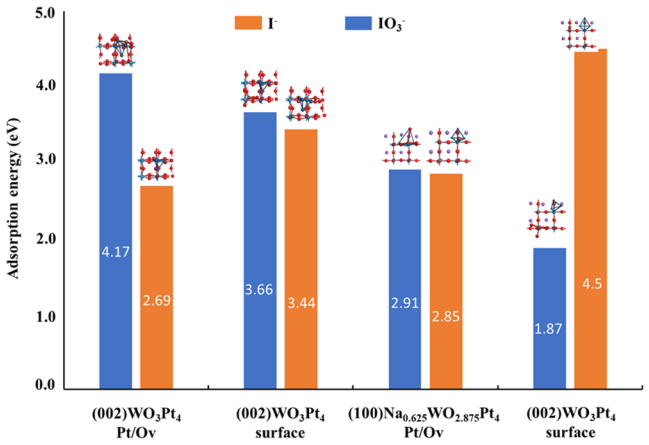

Figure 7. Adsorption energies and selected configurations of IO_3 and I adsorbed onto the surface of WO_3Pt_4 and $Na_{0.625}WO_{2.875}Pt_4$. Pt/Ov represents adsorption onto the Pt cluster, while surface represents adsorption onto the catalyst surface.

for the catalyst WO_3Pt_4, iodate is more easily adsorbed than iodide (in good agreement with experimental results). For the $Na_{0.625}WO_{2.875}Pt_4$ catalyst, it was found that both iodate and iodide were adsorbed onto the catalyst; however, iodide was adsorbed to a greater degree onto the catalyst. In each case, iodate adsorbed more preferentially onto the Pt cluster for subsequent reduction reactions, while iodide adsorbed more easily onto the catalyst surface for subsequent oxidation reactions. It should be noted that for both catalysts, the relaxation of iodate led to the stretching of the I═O bonds in every case, even when constraints were applied and, in most cases, the O atom dissociated. Overall, the DFT calculation results suggest that the preferential adsorption of IO_3^- on OEP and I^- on HEP would be the reason for the enhanced selective H_2 and O_2 evolution using the present Z-scheme.

We also attempted to realize a direct Z-scheme (in the absence of a redox couple, maybe a solid Z-scheme concept) by mixing 3%Pt-$Na_{0.56}WO_{3-x}$ and 0.5%Pt-WO_3 powders in an aqueous solution to produce H_2 and O_2, simultaneously. However, no gas evolution is noted (Table 1, run 11), suggesting that the simple physical mixing of the HEP and OEP powders cannot work well for water splitting herein, which is also useful for the separation of H_2 and O_2 production in two compartments based on the particle suspension Z-scheme rather than solid Z-scheme that produce mixed H_2 and O_2 in one cell.

Based on the above results, we proposed the reaction pathway for the new WOZ system schematically in Scheme 1,

Scheme 1. Proposed Reaction Pathway for the New WOZ Water Splitting System

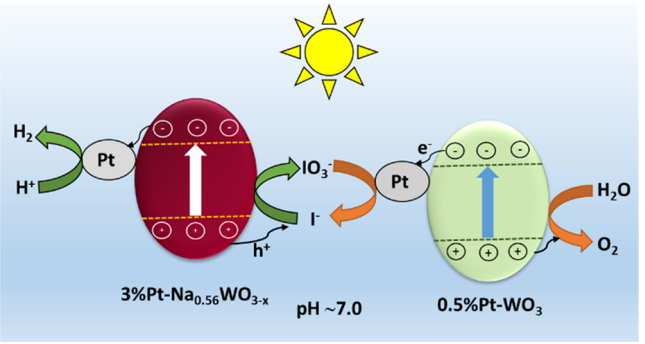

which is supported by the above investigation. The stoichiometric overall water splitting at pH 7.0 occurs in the presence of a redox mediator IO_3^-/I^-. Upon irradiation, photoexcited electrons from Pt-$Na_{0.56}WO_{3-x}$ transfer to Pt active sites, where proton reduction occurs to produce H_2, and the corresponding holes oxidize I^- ions into IO_3^-, which gets regenerated back to I^- by the photogenerated electrons on Pt-WO_3, while photogenerated holes on Pt-WO_3 perform water oxidation to generate O_2, resulting into a complete cycle.

3. CONCLUSIONS

In summary, we have demonstrated the original tungsten oxides-only suspension Z-scheme for efficient photocatalytic pure water splitting under the full-arc and visible light conditions in the presence of the IO_3^-/I^- redox couple. Such a design enables separately and readily optimization of each photocatalyst and the cocatalyst. So the stepwise independent H_2 and O_2 evolution half-reactions optimization was carried out to minimize/eliminate undesirable reactions. The band position measurements indicate a matched electronic structure for the new Z-scheme. Then, for the first time, the WO_3-based Z-scheme has been validated for visible-driven complete water splitting by a double excitation mechanism. This novel particulate WOZ exhibits 6.06% AQY at 420 nm when considering the electron number for H_2 production as 2. Furthermore, I^- was found to be favorably adsorbed on $Na_{0.56}WO_{3-x}$ and IO_3^- on WO_3 nanosheets by both experimental runs and theoretical modeling, being crucial

https://doi.org/10.1021/acscatal.3c01312
ACS Catal. 2023, 13, 9113−9124

for an efficient Z-scheme system. The low cost and ensured stability of tungsten oxides are also highly appropriate to subseqent scaling up.

4. EXPERIMENTAL SECTION

4.1. Materials and Reagents. Sodium tungstate dihydrate ($Na_2WO_4{\cdot}2H_2O$), sodium borohydride ($NaBH_4$), sodium iodide (NaI), and sodium iodate ($NaIO_3$) were purchased from Sigma Aldrich and used as received. All solutions were prepared using deionized (DI) water. Other chemicals used for experiments were purchased from commercial sources and used without further purification.

4.2. Synthesis of HEP. Sodium tungsten oxide bronze (Na_xWO_{3-x}) was synthesized by reducing the sodium tungstate dihydrate ($Na_2WO_4{\cdot}2H_2O$) using sodium borohydride ($NaBH_4$).[49] Briefly, 25 mL of 2.4 M $NaBH_4$ prepared in ice-cold water at pH >10 (essential to suppress the hydrogen evolution from $NaBH_4$ for upholding the reducing power) was added dropwise to 25 mL of 0.24 M $Na_2WO_4{\cdot}2H_2O$ solution (pH decreased to 6.5) under stirring. Simultaneously, 5 M HCl was added dropwise to the stirring solution to maintain the pH of ∼6.5 because the addition of $NaBH_4$ would raise the pH due to the formation of NaOH and $NaBO_2$. This mixture was stirred continuously for 2 h, resulting in a dark brown precipitate, which was kept undisturbed for 2 h for settling down the precipitate. Then, the suspension was centrifuged to separate the precipitate for 10 min at 9000 rpm (each run) and the residue was washed several times with water to remove unreacted precursors, followed by drying at 70 °C for 2 h in a vacuum oven. To obtain crystalline Na_xWO_{3-x}, the synthesized sample was annealed at 800 °C for 3 h (denoted $Na_{0.56}WO_{3-x}$) under a N_2 atmosphere in a tube furnace.

4.3. Synthesis of OEP. Two-dimensional (2D) tungstic acid ($WO_3{\cdot}H_2O$) nanosheets were synthesized as per the earlier report.[40] Briefly, 120 mM $Na_2WO_4{\cdot}2H_2O$ was prepared in 40 mL of DI water, and 4 mL of HCl was added in a dropwise manner while stirring for 1 h. The obtained pale green suspension was then centrifuged for 10 min at 9000 rpm (each run) to separate the precipitate, and the residue was washed several times with water to remove the unreacted precursors, followed by drying in an air oven at 70 °C overnight. The as-synthesized $WO_3{\cdot}H_2O$ nanosheets were annealed at 500 °C for 3 h in a muffle furnace at a heating rate of 10 °C min^{-1} to obtain monoclinic WO_3 nanosheets.

4.4. Platinum Cocatalyst Loading. A 3wt%Pt cocatalyst was loaded onto the $Na_{0.56}WO_{3-x}$ (HEP) surface and 0.5wt% Pt was loaded on WO_3 nanosheets (OEP) using a photodeposition method by continuous full-arc irradiation of the 10% aqueous methanol solution containing a $H_2PtCl_6{\cdot}6H_2O$ precursor for 1 h using a 300 W Xe lamp (*TrusTech PLS−SXE 300/300UV*). Later, the reaction mixture was centrifuged, followed by washing several times to remove the unreacted Pt precursors. Then, the residue was dried at 80 °C for 12 h under vacuum. The HEP photocatalyst was immediately used after the centrifugation.

4.5. Characterization. The X-ray diffraction (XRD) patterns were obtained using a STOE STADI-P diffractometer with Mo Kα as the X-ray radiation source. UV−Vis diffuse reflectance spectra (DRS) of the HEP and OEP powders were collected using an Agilent Cary 5000 spectrophotometer fitted with an integrating sphere using standard barium sulfate powder as a reference. TEM measurements were performed using a JEOL2100 TEM, operated at 200 kV. Samples for TEM measurements were prepared by drop-casting the dilute dispersions of the photocatalysts onto the carbon-coated copper grids. X-ray photoelectron spectroscopy (XPS) measurements were undertaken using a Kratos Axis SUPRA machine using monochromated Al-Kα irradiation as a source of X-rays. XPS data analysis was performed using Casa XPS software. Shirley/Touguard methods were used for background corrections. Raman spectra were measured on a Renishaw inVia Raman microscope, using a 532 nm excitation laser. The photoelectrochemical onset potential measurements were recorded using linear sweep voltammetry by sweeping the potential from +0.8 to −0.5 V vs Ag/AgCl in a conventional three-electrode (photocatalyst film-deposited electrode as the working electrode, Ag/AgCl as the reference electrode, and a platinum mesh as the counter electrode) cell using an electrochemical analyzer (IVIUM Technologies). A 0.1 M Na_2SO_4 (pH ∼7.0) solution was used as the electrolyte in the presence of 10% methanol as a hole scavenger. The photocatalyst film was prepared by dispersing 20 mg of the photocatalyst in a 5.4 mL solution comprising water:ethanol at a 4:1 (v/v) ratio and 0.4 mL of Nafion (5% solution), followed by 1 h ultrasonication. 50 μL of the obtained slurry was drop-cast onto the precleaned fluorine-doped tin oxide (FTO) conducting substrate, followed by drying at 60 °C in an oven before the electrochemical tests. The area of the photocatalyst thin film was 1 × 1 cm^2, whereas the size of the FTO substrate was 1 × 2 cm^2. The catalyst loading amount was ca. 3.7 mg mL^{-1}.

4.6. Photocatalytic Studies. The H_2 and O_2 evolution half-reactions and their simultaneous production in a Z-scheme system were carried out in a custom-made glass batch reactor with a top quartz window. The known amount of photocatalysts was loaded in the reactor containing 70 mL of water and 5 mM NaI and dispersed well by ultrasonication for 30 min. The pH of the solution was controlled by adding dilute solutions of H_2SO_4 and NaOH. The reactor was sealed and purged with high-purity Ar gas for 1 h to remove air/dissolved oxygen in the solution and headspace. After baseline measurement (0 h), the reactor was irradiated using a 300 W Xe lamp (Newport). The reactor was placed in a water bath during irradiation to maintain the reaction temperature. The production of H_2 and O_2 gases was quantified at regular intervals using gas chromatography (Varian 430-GC, TCD, argon carrier gas) equipped with a molecular 5A column using Ar as the carrier gas and N_2 as the internal reference. The apparent quantum yield (AQY) was determined by performing photocatalytic experiments at specific wavelengths by using an appropriate bandpass filter. For AQY measurements, 60 mg of HEP and 30 mg of OEP were dispersed in 70 mL of water containing 5 mM NaI. The reactor was irradiated through a 2 cm diameter aperture, enabling the central beam through, which is very reliable for the AQY analysis as highlighted by Domen et al.[50] The light intensity of the lamp was measured at five different points to obtain an average intensity using a calibrated photodiode coupled with an optical power meter (Newport, Model 1908-R). The measured light intensity with a 420 nm bandpass filter was 0.5 mW cm^{-2}. The AQY was calculated (see Supporting Information for detailed calculation) using the following equation

$$\mathrm{AQY}(\%) = \frac{\alpha \times \textit{amount of gas molecules evolved}}{\textit{Total number of incident photons}} \times 100\% \quad (10)$$

https://doi.org/10.1021/acscatal.3c01312
ACS Catal. 2023, 13, 9113−9124

where α = 2 and 4 for H_2 and O_2 evolution reactions provided that there are 2 electrons required for one H_2 molecule production and 4 holes for one O_2 molecule production, respectively. The GC calibration curves for H_2 and O_2 are provided in Figure S32. Furthermore, the raw GC chromatograms for the Z-scheme water splitting, under a full-arc condition, corresponding to the gas evolution shown in Figure 5a, are given in Figure S33.

4.7. Adsorption Study. The adsorption of I^- and IO_3^- ions on the surface of the HEP and OEP was studied by measuring their concentrations using UV−Vis absorption spectroscopy. The determination of the I^- ion concentration is straightforward as it can show the absorption peak at 225 nm without adding any reagent. However, IO_3^- shows absorption peaks at 288 and 352 nm only in the presence of an excess of I^- and 0.2 M H_2SO_4. The calibration curves for I^- and IO_3^- are shown in Figures S34 and S35, respectively. We monitored the peak at 352 nm to determine the concentration of IO_3^-.

4.8. Computational Details. Density functional theory (DFT) calculations were carried out to investigate the adsorption of IO_3^- and I^- onto both WO_3Pt_4 and $Na_{0.625}WO_{2.875}Pt_4$. The structure of $Na_{0.625}WO_{2.875}Pt_4$, through XRD analysis, was deemed to be structurally similar enough to the experimentally investigated $Na_{0.56}WO_{3-x}$. For the adsorption calculations, BIOVIA Materials Studio (MS) package was used with the generalized gradient approximation (GGA) and Perdew−Burke−Ernzerhof (PBE) functional to account for the exchange-correlation energy.[51] All calculations were spin-polarized, with the projector augmented wave (PAW) pseudopotentials and the Van der Waals interactions were described by the Grimme DFT-D3 method.[52] The Kohn−Sham equations were solved with a convergence criterion of 2.0e-5 eV/atom for energy and 0.05 eV $Å^{-1}$. Additionally, *k*-point sampling was carried out using the Monkhorst−Pack scheme with a (1 ×1 × 1) grid, and a cutoff energy of 489.8 eV was used.

■ ASSOCIATED CONTENT

Supporting Information

The Supporting Information is available free of charge at https://pubs.acs.org/doi/10.1021/acscatal.3c01312.

Structural representation of materials; SEM, TEM, and EDX of HEP and OEP; XRD, and XPS data before and after photocatalysis; UV−Vis of HEP and OEP; photoelectrochemical onset potential measurements; Mott−Schottky measurements; pH optimization; H_2 evolution activity at longer wavelengths; control experiments; AQY comparison with optical spectra of HEP and OEP; DFT results; GC calibration and raw data; and adsorption of I^- and IO_3^- (PDF)

■ AUTHOR INFORMATION

Corresponding Authors

Xiaolei Zhang − *Department of Chemical and Process Engineering, University of Strathclyde, Glasgow G1 1XL, U.K.*; Email: xiaolei.zhang@strath.ac.uk

Junwang Tang − *Department of Chemical Engineering, University College London, London WC1E 7JE, U.K.*; orcid.org/0000-0002-2323-5510; Email: junwang.tang@ucl.ac.uk

Authors

Madasamy Thangamuthu − *Department of Chemical Engineering, University College London, London WC1E 7JE, U.K.*; Present Address: School of Chemistry, University of Nottingham, Nottingham NG7 2RD, UK; orcid.org/0000-0001-8391-3769

Kiran Vankayala − *Department of Chemical Engineering, University College London, London WC1E 7JE, U.K.*; Present Address: Department of Chemistry, Birla Institute of Science & Technology, Pilani, K. K. Birla Goa campus, Goa 403726, India; orcid.org/0000-0002-1910-696X

Lunqiao Xiong − *Department of Chemical Engineering, University College London, London WC1E 7JE, U.K.*; orcid.org/0000-0003-2963-9863

Stuart Conroy − *Department of Chemical and Process Engineering, University of Strathclyde, Glasgow G1 1XL, U.K.*

Complete contact information is available at: https://pubs.acs.org/10.1021/acscatal.3c01312

Author Contributions

[⊥]M.T. and K.V. contributed equally. The manuscript was written through contributions of all authors. All authors have given approval to the final version of the manuscript.

Notes

The authors declare no competing financial interest.

■ ACKNOWLEDGMENTS

The authors acknowledge the UK EPSRC (EP/S018204/2), Leverhulme Trust (RPG-2017-122), Royal Society Newton Advanced Fellowship grant (NAF\R1\191163), and Royal Society Leverhulme Trust Senior Research Fellowship (SRF \R1\21000153). XPS data collection was performed at the EPSRC National Facility for XPS ("HarwellXPS"), operated by Cardiff University and UCL, under Contract No. PR16195. The authors also thank Dr Jijia Xie, Ms Hui Wang, and Jianfeng Ye for constructive discussion on the experimental design.

■ REFERENCES

(1) Pareek, A.; Dom, R.; Gupta, J.; Chandran, J.; Adepu, V.; Borse, P. H. Insights into Renewable Hydrogen Energy: Recent Advances and Prospects. *Mater. Sci. Energy Technol.* **2020**, *3*, 319−327.

(2) Smith, C.; Hill, A. K.; Torrente-Murciano, L. Current and Future Role of Haber−Bosch Ammonia in a Carbon-Free Energy Landscape. *Energy Environ. Sci.* **2020**, *13*, 331−344.

(3) Sobrino, F. H.; Monroy, C. R.; Pérez, J. L. H. Critical Analysis on Hydrogen as an Alternative to Fossil Fuels and Biofuels for Vehicles in Europe. *Renewable Sustainable Energy Rev.* **2010**, *14*, 772−780.

(4) Wang, Q.; Domen, K. Particulate Photocatalysts for Light-Driven Water Splitting: Mechanisms, Challenges, and Design Strategies. *Chem. Rev.* **2020**, *120*, 919−985.

(5) Wang, Y.; Vogel, A.; Sachs, M.; Sprick, R. S.; Wilbraham, L.; Moniz, S. J. A.; Godin, R.; Zwijnenburg, M. A.; Durrant, J. R.; Cooper, A. I.; Tang, J. Current Understanding and Challenges of Solar-Driven Hydrogen Generation Using Polymeric Photocatalysts. *Nat. Energy* **2019**, *4*, 746−760.

(6) Maeda, K.; Teramura, K.; Lu, D.; Takata, T.; Saito, N.; Inoue, Y.; Domen, K. Photocatalyst Releasing Hydrogen from Water. *Nature* **2006**, *440*, 295.

(7) Tan, H. L.; Amal, R.; Ng, Y. H. Alternative Strategies in Improving the Photocatalytic and Photoelectrochemical Activities of Visible Light-Driven BiVO4: A Review. *J. Mater. Chem. A* **2017**, *5*, 16498−16521.

(8) Quan, H.; Gao, Y.; Wang, W. Tungsten Oxide-Based Visible Light-Driven Photocatalysts: Crystal and Electronic Structures and Strategies for Photocatalytic Efficiency Enhancement. *Inorg. Chem. Front.* **2020**, *7*, 817−838.
(9) Moniz, S. J. A.; Shevlin, S. A.; Martin, D. J.; Guo, Z.-X.; Tang, J. Visible-Light Driven Heterojunction Photocatalysts for Water Splitting − a Critical Review. *Energy Environ. Sci.* **2015**, *8*, 731−759.
(10) Kato, H.; Sasaki, Y.; Shirakura, N.; Kudo, A. Synthesis of Highly Active Rhodium-Doped SrTiO3 Powders in Z-Scheme Systems for Visible-Light-Driven Photocatalytic Overall Water Splitting. *J. Mater. Chem. A* **2013**, *1*, 12327−12333.
(11) Wang, Y.; Suzuki, H.; Xie, J.; Tomita, O.; Martin, D. J.; Higashi, M.; Kong, D.; Abe, R.; Tang, J. Mimicking Natural Photosynthesis: Solar to Renewable H2 Fuel Synthesis by Z-Scheme Water Splitting Systems. *Chem. Rev.* **2018**, *118*, 5201−5241.
(12) Hisatomi, T.; Domen, K. Reaction Systems for Solar Hydrogen Production via Water Splitting with Particulate Semiconductor Photocatalysts. *Nat. Catal.* **2019**, *2*, 387−399.
(13) Pinaud, B. A.; Benck, J. D.; Seitz, L. C.; Forman, A. J.; Chen, Z.; Deutsch, T. G.; James, B. D.; Baum, K. N.; Baum, G. N.; Ardo, S.; Wang, H.; Miller, E.; Jaramillo, T. F. Technical and Economic Feasibility of Centralized Facilities for Solar Hydrogen Production via Photocatalysis and Photoelectrochemistry. *Energy Environ. Sci.* **2013**, *6*, 1983−2002.
(14) Wang, Q.; Okunaka, S.; Tokudome, H.; Hisatomi, T.; Nakabayashi, M.; Shibata, N.; Yamada, T.; Domen, K. Printable Photocatalyst Sheets Incorporating a Transparent Conductive Mediator for Z-Scheme Water Splitting. *Joule* **2018**, *2*, 2667−2680.
(15) Idriss, H. The Elusive Photocatalytic Water Splitting Reaction Using Sunlight on Suspended Nanoparticles: Is There a Way Forward? *Catal.: Sci. Technol.* **2020**, *10*, 304−310.
(16) Maeda, K. Z-Scheme Water Splitting Using Two Different Semiconductor Photocatalysts. *ACS Catal.* **2013**, *3*, 1486−1503.
(17) Chen, S.; Takata, T.; Domen, K. Particulate Photocatalysts for Overall Water Splitting. *Nat. Rev. Mater.* **2017**, *2*, 17050.
(18) Abe, R.; Shinmei, K.; Koumura, N.; Hara, K.; Ohtani, B. Visible-Light-Induced Water Splitting Based on Two-Step Photoexcitation between Dye-Sensitized Layered Niobate and Tungsten Oxide Photocatalysts in the Presence of a Triiodide/Iodide Shuttle Redox Mediator. *J. Am. Chem. Soc.* **2013**, *135*, 16872−16884.
(19) Nishioka, S.; Hojo, K.; Xiao, L.; Gao, T.; Miseki, Y.; Yasuda, S.; Yokoi, T.; Sayama, K.; Mallouk, T. E.; Maeda, K. Surface-Modified, Dye-Sensitized Niobate Nanosheets Enabling an Efficient Solar-Driven Z-Scheme for Overall Water Splitting. *Sci. Adv.* **2023**, *8*, No. eadc9115.
(20) Abe, R.; Sayama, K.; Domen, K.; Arakawa, H. A New Type of Water Splitting System Composed of Two Different TiO2 Photocatalysts (Anatase, Rutile) and a IO3−/I− Shuttle Redox Mediator. *Chem. Phys. Lett.* **2001**, *344*, 339−344.
(21) Konta, R.; Ishii, T.; Kato, H.; Kudo, A. Photocatalytic Activities of Noble Metal Ion Doped SrTiO3 under Visible Light Irradiation. *J. Phys. Chem. B* **2004**, *108*, 8992−8995.
(22) Martin, D. J.; Reardon, P. J. T.; Moniz, S. J. A.; Tang, J. Visible Light-Driven Pure Water Splitting by a Nature-Inspired Organic Semiconductor-Based System. *J. Am. Chem. Soc.* **2014**, *136*, 12568−12571.
(23) Maeda, K.; Lu, D.; Domen, K. Solar-Driven Z-Scheme Water Splitting Using Modified BaZrO3−BaTaO2N Solid Solutions as Photocatalysts. *ACS Catal.* **2013**, *3*, 1026−1033.
(24) Chen, S.; Qi, Y.; Hisatomi, T.; Ding, Q.; Asai, T.; Li, Z.; Ma, S. S. K.; Zhang, F.; Domen, K.; Li, C. Efficient Visible-Light-Driven Z-Scheme Overall Water Splitting Using a MgTa2O6−xNy /TaON Heterostructure Photocatalyst for H2 Evolution. *Angew. Chem., Int. Ed.* **2015**, *54*, 8498−8501.
(25) Kato, T.; Hakari, Y.; Ikeda, S.; Jia, Q.; Iwase, A.; Kudo, A. Utilization of Metal Sulfide Material of (CuGa)1−XZn2xS2 Solid Solution with Visible Light Response in Photocatalytic and Photoelectrochemical Solar Water Splitting Systems. *J. Phys. Chem. Lett.* **2015**, *6*, 1042−1047.
(26) Iwashina, K.; Iwase, A.; Ng, Y. H.; Amal, R.; Kudo, A. Z-Schematic Water Splitting into H2 and O2 Using Metal Sulfide as a Hydrogen-Evolving Photocatalyst and Reduced Graphene Oxide as a Solid-State Electron Mediator. *J. Am. Chem. Soc.* **2015**, *137*, 604−607.
(27) Miseki, Y.; Fujiyoshi, S.; Gunji, T.; Sayama, K. Photocatalytic Z-Scheme Water Splitting for Independent H2/O2 Production via a Stepwise Operation Employing a Vanadate Redox Mediator under Visible Light. *J. Phys. Chem. C* **2017**, *121*, 9691−9697.
(28) Qi, Y.; Chen, S.; Li, M.; Ding, Q.; Li, Z.; Cui, J.; Dong, B.; Zhang, F.; Li, C. Achievement of Visible-Light-Driven Z-Scheme Overall Water Splitting Using Barium-Modified Ta3N5 as a H2-Evolving Photocatalyst. *Chem. Sci.* **2017**, *8*, 437−443.
(29) Dong, B.; Qi, Y.; Cui, J.; Liu, B.; Xiong, F.; Jiang, X.; Li, Z.; Xiao, Y.; Zhang, F.; Li, C. Synthesis of BaTaO2N Oxynitride from Ba-Rich Oxide Precursor for Construction of Visible-Light-Driven Z-Scheme Overall Water Splitting. *Dalton Trans.* **2017**, *46*, 10707−10713.
(30) Thangamuthu, M.; Ruan, Q.; Ohemeng, P. O.; Luo, B.; Jing, D.; Godin, R.; Tang, J. Polymer Photoelectrodes for Solar Fuel Production: Progress and Challenges. *Chem. Rev.* **2022**, *122*, 11778−11829.
(31) Ma, J.; Miao, T. J.; Tang, J. Charge Carrier Dynamics and Reaction Intermediates in Heterogeneous Photocatalysis by Time-Resolved Spectroscopies. *Chem. Soc. Rev.* **2022**, *51*, 5777−5794.
(32) Wang, Y.; Chen, E.; Tang, J. Insight on Reaction Pathways of Photocatalytic CO2 Conversion. *ACS Catal.* **2022**, *12*, 7300−7316.
(33) Wang, Y.; Liu, T.; Li, H.; Liu, B.; Yang, L. Tungsten-Based Photocatalysts with UV−Vis−NIR Photocatalytic Capacity: Progress and Opportunity. *Tungsten* **2019**, *1*, 247−257.
(34) Huang, Z.-F.; Song, J.; Pan, L.; Zhang, X.; Wang, L.; Zou, J.-J. Tungsten Oxides for Photocatalysis, Electrochemistry, and Phototherapy. *Adv. Mater.* **2015**, *27*, 5309−5327.
(35) Paik, T.; Cargnello, M.; Gordon, T. R.; Zhang, S.; Yun, H.; Lee, J. D.; Woo, H. Y.; Oh, S. J.; Kagan, C. R.; Fornasiero, P.; Murray, C. B. Photocatalytic Hydrogen Evolution from Substoichiometric Colloidal WO3−x Nanowires. *ACS Energy Lett.* **2018**, *3*, 1904−1910.
(36) Wang, L.; Tsang, C.-S.; Liu, W.; Zhang, X.; Zhang, K.; Ha, E.; Kwok, W.-M.; Park, J. H.; Suk Lee, L. Y.; Wong, K.-Y. Disordered Layers on WO3 Nanoparticles Enable Photochemical Generation of Hydrogen from Water. *J. Mater. Chem. A* **2019**, *7*, 221−227.
(37) Azimirad, R.; Akhavan, O.; Moshfegh, A. Z. Simple Method to Synthesize NaxWO3 Nanorods and Nanobelts. *J. Phys. Chem. C* **2009**, *113*, 13098−13102.
(38) Brown, B. W.; Banks, E. The Sodium Tungsten Bronzes1,2. *J. Am. Chem. Soc.* **1954**, *76*, 963−966.
(39) Lee, W. H.; Hwang, H.; Moon, K.; Shin, K.; Han, J. H.; Um, S. H.; Park, J.; Cho, J. H. Increased Environmental Stability of a Tungsten Bronze NIR-Absorbing Window. *Fibers Polym.* **2013**, *14*, 2077−2082.
(40) Nayak, A. K.; Lee, S.; Choi, Y. I.; Yoon, H. J.; Sohn, Y.; Pradhan, D. Crystal Phase and Size-Controlled Synthesis of Tungsten Trioxide Hydrate Nanoplates at Room Temperature: Enhanced Cr(VI) Photoreduction and Methylene Blue Adsorption Properties. *ACS Sustainable Chem. Eng.* **2017**, *5*, 2741−2750.
(41) Liu, J.; Han, L.; An, N.; Xing, L.; Ma, H.; Cheng, L.; Yang, J.; Zhang, Q. Enhanced Visible-Light Photocatalytic Activity of Carbonate-Doped Anatase TiO2 Based on the Electron-Withdrawing Bidentate Carboxylate Linkage. *Appl. Catal., B* **2017**, *202*, 642−652.
(42) Wang, P.-Q.; Bai, Y.; Luo, P.-Y.; Liu, J.-Y. Graphene−WO3 Nanobelt Composite: Elevated Conduction Band toward Photocatalytic Reduction of CO2 into Hydrocarbon Fuels. *Catal. Commun.* **2013**, *38*, 82−85.
(43) Kudo, A.; Omori, K.; Kato, H. A Novel Aqueous Process for Preparation of Crystal Form-Controlled and Highly Crystalline BiVO4 Powder from Layered Vanadates at Room Temperature and Its Photocatalytic and Photophysical Properties. *J. Am. Chem. Soc.* **1999**, *121*, 11459−11467.

https://doi.org/10.1021/acscatal.3c01312
ACS Catal. 2023, 13, 9113−9124

(44) Dunkle, S. S.; Helmich, R. J.; Suslick, K. S. BiVO4 as a Visible-Light Photocatalyst Prepared by Ultrasonic Spray Pyrolysis. *J. Phys. Chem. C* **2009**, *113*, 11980−11983.
(45) Yang, Y.; Chen, J.; Liu, X.; Qiu, M.; Liu, L.; Gao, F. Oxygen Vacancy-Mediated WO3 Nanosheets by Etched {200} Facets and the Efficient Visible-Light Photocatalytic Oxygen Evolution. *New J. Chem.* **2019**, *43*, 16391−16395.
(46) Ohno, T.; Saito, S.; Fujihara, K.; Matsumura, M. Photocatalyzed Production of Hydrogen and Iodine from Aqueous Solutions of Iodide Using Platinum-Loaded TiO2 Powder. *Bull. Chem. Soc. Jpn.* **1996**, *69*, 3059−3064.
(47) Wang, Q.; Hisatomi, T.; Jia, Q.; Tokudome, H.; Zhong, M.; Wang, C.; Pan, Z.; Takata, T.; Nakabayashi, M.; Shibata, N.; Li, Y.; Sharp, I. D.; Kudo, A.; Yamada, T.; Domen, K. Scalable Water Splitting on Particulate Photocatalyst Sheets with a Solar-to-Hydrogen Energy Conversion Efficiency Exceeding 1%. *Nat. Mater.* **2016**, *15*, 611−615.
(48) Abe, R.; Higashi, M.; Domen, K. Overall Water Splitting under Visible Light through a Two-Step Photoexcitation between TaON and WO3 in the Presence of an Iodate−Iodide Shuttle Redox Mediator. *ChemSusChem* **2011**, *4*, 228−237.
(49) Tsang, C.; Lai, S. Y.; Manthiram, A. Reduction of Aqueous Na2WO4 by NaBH4 at Ambient Temperatures To Obtain Lower Valent Tungsten Oxides. *Inorg. Chem.* **1997**, *36*, 2206−2210.
(50) Takata, T.; Jiang, J.; Sakata, Y.; Nakabayashi, M.; Shibata, N.; Nandal, V.; Seki, K.; Hisatomi, T.; Domen, K. Photocatalytic Water Splitting with a Quantum Efficiency of Almost Unity. *Nature* **2020**, *581*, 411−414.
(51) Perdew, J. P.; Burke, K.; Ernzerhof, M. Generalized Gradient Approximation Made Simple. *Phys. Rev. Lett.* **1996**, *77*, 3865−3868.
(52) Grimme, S.; Antony, J.; Ehrlich, S.; Krieg, H. A Consistent and Accurate Ab Initio Parametrization of Density Functional Dispersion Correction (DFT-D) for the 94 Elements H-Pu. *J. Chem. Phys.* **2010**, *132*, No. 154104.

https://doi.org/10.1021/acscatal.3c01312
ACS Catal. 2023, 13, 9113−9124